Inorganic Chemistry
Article
pubs.acs.org/IC

Molecular and Electronic Structures of Complexes Containing 1-(2-pyridylazo)-2-phenanthrol (PAPL): Revisiting a Redox-Active Ligand

Natasha Van Damme,[†] Alan J. Lough,[‡] Serge I. Gorelsky,[§] and Martin T. Lemaire*,[†]

[†]Department of Chemistry, Brandon University, Brandon, Manitoba R7A 6A9, Canada
[‡]Department of Chemistry, University of Toronto, Toronto, Ontario M5S 3H6, Canada
[§]Center for Catalysis Research and Innovation, Department of Chemistry, University of Ottawa, Ottawa, Ontario K1N 6N5, Canada

Supporting Information

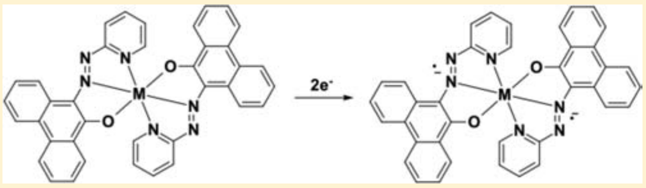

ABSTRACT: Herein we report the molecular structures and electronic properties of neutral, homoleptic, six-coordinate complexes of the general formula $M(PAPL)_2$, where PAPL is the monoanion of 1-(2-pyridylazo)-2-phenanthrol (M = Mn, Ni, Zn). Although, the coordination chemistry of PAPL has been investigated in a few previous reports in the 1970s and 1980s, there are, to our knowledge, no reported single crystal X-ray diffraction studies of any complexes, or any other electronic property or computational studies of complexes containing the PAPL anion until now. The electronic structures of the complexes are probed with a combination of cyclic voltammetry, UV−vis spectroscopy, and spectroelectrochemical measurements. Density functional theory calculations support the redox-active nature of the PAPL ligand. In all complexes we observe two reversible ligand-centered reduction processes, suggesting it may be possible to access the open-shell radical-anionic state of the ligand.

INTRODUCTION

Molecular coordination complexes containing redox-active ligands (RALs) are of interest for application in small molecule catalytic transformations,[1] for the study of reactivity in metalloenzyme systems,[2] and for the possibility of future uses in molecule-based electronics or spintronics.[3] In particular azo-aromatic based systems have received much attention as facile reduction of the energetically low lying azo-centered π^* molecular orbital can produce radical anionic species, in addition to the variety of other uses of azo compounds, including as dyes and pigments.[4] Transition metal complexes of azo-aromatic ligands have been extensively reviewed by Goswami.[5] In particular, the ligands outlined in Figure 1 (right) have been coordinated to a wide range of transition metal ions to produce complexes with both closed- and open-shell ligands. Of interest to us are the homoleptic complexes containing tridentate ligands R = H, CH_3 reported with paramagnetic transition metal ions, such as Cr^{3+}, Mn^{2+}, Fe^{3+}, and Ni^{2+}.[4c,6] These complexes often feature reversible cathodic electrochemistry, suggesting stable ligand-centered reductions. Other complexes with these ligands have been reported with Mo, W, Rh, Re, Ru, and Os.[5]

Our interest in azo-aromatic ligands is focused on the study of magnetic exchange interactions in reduced azo-aromatic transition metal or lanthanide complexes and identifying new families of materials that exhibit reversible intramolecular electron transfer processes (redox-induced electron transfer or valence-tautomerism, as examples). In this regard we have identified the PAPL ligand [1-(2-pyridylazo)-2-phenanthrol, Figure 1] as a target system with a structure amenable to metal coordination as a tridentate anion, including N_{azo} coordination. The PAPL ligand structure appears to offer unusual redox activity in that either one-electron reduction (azo) or oxidation (phenoxyl) of the ligand could produce a metal coordinated radical. Also, the 9,10-phenanthrenequinone precursor to the PAPL ligand is readily substituted via simple electrophilic aromatic substitution reactions, which allows for other synthetic opportunities. The PAPL ligand was first reported by Chiswell and co-workers in 1963, and a handful of reports over the 1970s and 1980s document the preparation and electronic spectra of first, second, and some third row transition metal−PAPL complexes.[7,8] Since the mid-1980s, the chemistry of PAPL has been largely neglected with the exception of a few patents, and to our knowledge, there is no structural data reported from X-ray diffraction experiments for any of the reported metal−PAPL complexes. Nor is there any computational work outlining the electronic structure of these complexes, and we could find only two reports focused on the electrochemical properties of cobalt−PAPL complexes and electronic spectra of metal−PAPL complexes.[8d,h] In general, other PAPL-type ligands bearing other aryl substituents, such as phenol or napthol, in place of the phenanthrol ring, while known, have also not been thoroughly investigated in terms of their electronic or spectroscopic properties.[9] Our objective was to revisit the PAPL family of complexes and explore in more detail their structural and electronic properties. The anticipated redox active nature of the PAPL ligand would appear to have much to offer to the general area of RAL chemistry. Herein we report single-crystal X-ray diffraction data for three $M(PAPL)_2$

Received: June 27, 2013
Published: October 30, 2013

dx.doi.org/10.1021/ic401618u | *Inorg. Chem.* 2013, 52, 13021−13028

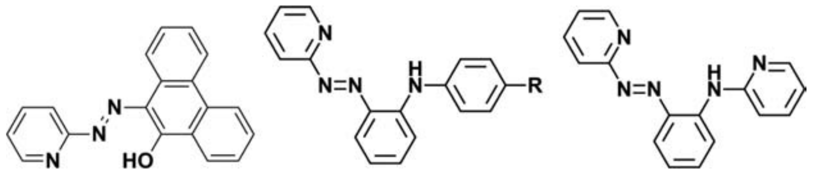

Figure 1. Left: 1-(2-Pyridylazo)-2-phenanthrol (PAPL). Right: Other 2-(arylazo)pyridine ligands reported by Goswami et al. (R = H, Cl, or CH_3).

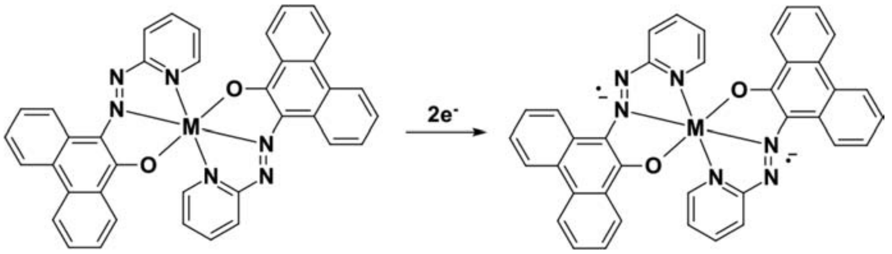

Figure 2. Left: Line drawing of the neutral $M(PAPL)_2$ complexes isolated in this work. Right: The anticipated two-electron reduction product of the neutral $M(PAPL)_2$ complex.

coordination complexes as well as a detailed look at the electronic structure of $M(PAPL)_2$ complexes (Figure 2) by an examination of electronic spectra and electrochemical and spectroelectrochemical experiments. Included are density functional theory calculations to support the experimental data provided.

■ EXPERIMENTAL SECTION

General Considerations. All reagents were commercially available and used as received unless otherwise stated. Deaerated and anhydrous solvents were obtained from a Puresolve PS MD-4 solvent purification system. $^1H/^{13}C$ NMR spectra were recorded on a Bruker Avance 400 MHz spectrometer with a 7.05 T Ultrashield magnet using deuterated solvents. FT-IR spectra were recorded on a Shimadzu IRAffinity spectrometer as KBr discs. UV−vis measurements were recorded on a Shimadzu 3600 UV−vis−NIR spectrophotometer in CH_2Cl_2 solution using quartz or infrasil cuvette cells. Elemental analyses were carried out by Canadian Microanalytical Services, Ltd., Delta, BC, Canada. Cyclic voltammetry (CV) experiments were performed with a Bioanalytical Systems Inc. (BASI) Epsilon electrochemical workstation. Compounds were dissolved in anhydrous solvent (CH_3CN), and then deaerated by sparging with N_2 gas for 10 min. Solution concentrations were approximately 10^{-3} M in analyte containing 0.5 M supporting electrolyte (Bu_4NPF_6). A typical three-electrode setup was used including a platinum working electrode, Ag/AgCl reference electrode, and a platinum wire auxiliary electrode. The scan rate for all CV experiments was 100 mV/s, unless noted otherwise. Spectroelectrochemical experiments were performed in dry, deoxygenated acetonitrile using a BASI spectroelectrochemical cell kit, including a thin-layer quartz cuvette, platinum minigrid working electrode, platinum wire counter electrode, and a Ag/AgCl reference electrode. Solutions were approximately 10^{-3} M containing 0.5 M Bu_4NPF_6. Potentials applied (−1.0, −1.2, and −1.5 V) were based on data obtained from CV experiments.

Computational Details. All DFT calculations were performed using the Gaussian 09 package[10] using the B3LYP hybrid functional[11,12] and the TZVP basis set[13] for all atoms. Tight SCF convergence criteria were used for all calculations. For each given spin state, the structures were optimized. The converged wave functions were tested to confirm that they correspond to the ground-state surface. The evaluation of atomic charges and spin densities was performed using the natural population analysis (NPA).[14] The generation of initial guess wave functions for the spin states with the antiferromagnetic coupling, the analysis of molecular orbitals in terms of fragment orbital contributions, and Mayer bond order calculations[15,16] were carried out using the AOMix program.[17,18] Time-dependent DFT (TD-DFT) calculations at the B3LYP/TZVP level were performed to calculate the absorption spectra as previously described.[18]

Synthesis. *1-(2-Pyridylazo)-2-phenanthrol (PAPL) (**1**).* 9,10-Phenanthrenequinone (0.27 g, 1.3 mmol) was combined with glacial acetic acid (10 mL) and heated (approximately 60 °C) for 15 min. Added dropwise to this hot solution was a slurry of 2-hydrazinopyridine (0.50 g, 4.6 mmol) in glacial acetic acid (2 mL). The reaction mixture was heated to reflux with stirring for 1.5 h and cooled to room temperature, and then the reaction contents were poured over ice. Neutralization with solid K_2CO_3 resulted in the generation of a bright orange precipitate, which was isolated by vacuum filtration (0.51 g, 70% yield). Characterization of **1** was nearly identical to reported values.[7,8c]

*$M(PAPL)_2$ [M = Mn (**2**), Ni (**3**), Zn (**4**)].* Compound **1** (0.50 g, 1.7 mmol) was dissolved in $CHCl_3$ (13 mL) and was combined with a MeOH (13 mL) solution containing 0.85 mmol $M(OAc)_2 \cdot H_2O$. The reaction mixtures were stirred at room temperature for 1 h, left to stand for 0.5 h, and then immersed in ice/water baths. The dark microcrystalline precipitates were isolated by vacuum filtration, washed with cold methanol, and then dried. Data for $Mn(PAPL)_2$ (**2**) follow. Yield (0.22 g, 40%). FT-IR (KBr): 3061(w), 1599(m), 1582(m), 1558(m), 1510(m), 1495(m), 1437(m), 1346(s), 1325(s), 1273(s), 1248(s), 1221(s), 1179(s), 1165(s), 1142(s), 1123(s), 1098(s), 1043(w), 1001(m), 926(m), 781(w), 756(m), 725(m) cm^{-1}. UV−vis (CH_2Cl_2) λ_{max} ($\varepsilon \times 10^4$) = 552 (4.1), 514 (3.6), 484 nm (3.0 cm^{-1} M^{-1}). Anal. Calcd for (%) $C_{38}H_{24}N_6O_2Mn$ (Found %): C, 70.03 (69.95); H, 3.71 (3.77); N, 12.90 (12.38). Crystals suitable for X-ray diffraction were grown by diffusion of diethyl ether into a $CHCl_3$ solution of **2**. Data for $Ni(PAPL)_2$ (**3**) follow. Yield (0.29 g, 53%). FT-IR (KBr): 3059(w), 1603(m), 1584(m), 1560(m), 1526(m), 1512(m), 1495(m), 1443(m), 1368(s), 1346(s), 1327(s), 1275(s), 1250(s), 1223(s), 1184(s), 1166(m), 1144(s), 1126(m), 1099(m), 1009(m), 928(m), 754(m), 725(m) cm^{-1}. UV−vis (CH_2Cl_2) λ_{max} ($\varepsilon \times 10^4$) = 555 (6.6), 517 nm (5.2 cm^{-1} M^{-1}). Anal. Calcd for (%) $C_{38}H_{24}N_6O_2Ni$ (Found %): C, 69.63 (69.69); H, 3.69 (3.69); N, 12.83 (12.28). Crystals suitable for X-ray diffraction were grown by diffusion of *n*-pentane into a THF solution of **3**. Data for $Zn(PAPL)_2$ (**4**) follow. Yield (0.26 g, 48%). FT-IR (KBr): 3063(w), 1603(m), 1584(m), 1560(m), 1526(m), 1497(m), 1468(m), 1443(m), 1371(s), 1348(s), 1327(s), 1275(s), 1254(s), 1221(s), 1182(s), 1167(m), 1142(s), 1122(m). 1099(m), 1005(m), 928(m), 756(m), 725(m) cm^{-1}. UV−vis (CH_2Cl_2) λ_{max} ($\varepsilon \times 10^4$) = 544 (6.9), 508 nm (4.4 cm^{-1} M^{-1}). Anal. Calcd for (%) $C_{38}H_{24}N_6O_2Zn$ (Found %): C, 68.92 (69.67); H, 3.66 (3.52); N, 12.70 (12.40). Crystals suitable for X-ray diffraction were grown by diffusion of diethyl ether into a $CHCl_3$ solution of **4**. Crystal data are presented in Table 1.

Table 1. Crystallographic Data for 2−4

	2	3	4
formula	$C_{38}H_{24}MnN_6O_2$	$C_{42}H_{32}N_6NiO_3$	$C_{42}H_{34}N_6O_3Zn$
fw	651.57	727.45	736.12
dimensions (mm^3)	0.12 × 0.11 × 0.08	0.17 × 0.10 × 0.01	0.23 × 0.09 × 0.03
a (Å)	13.1386(5)	22.6908(10)	13.1546(12)
b (Å)	22.2937(9)	12.9710(6)	22.634(2)
c (Å)	13.1559(5)	22.7828(10)	13.0599(11)
cryst syst	monoclinic	orthorhombic	monoclinic
α (deg)	90	90	90
β (deg)	118.313(2)	90	119.539(3)
γ (deg)	90	90	90
V ($Å^3$)	3392.5(2)	6705.5(5)	3383.0(5)
space group	$P2_1/c$	$Pbcn$	$P2_1/c$
Z	4	8	4
μ (mm^{-1})	3.499	1.254	1.423
T (K)	147(2)	147(2)	147(2)
indep reflns	5817	5666	5823
no. params	424	469	478
R1	0.0413	0.0526	0.0363
wR2	0.1057	0.1340	0.0934

■ RESULTS AND DISCUSSION

Coordination Chemistry and Single Crystal X-ray Diffraction Studies. Ligand PAPL **1** is easily prepared as per Chiswell or Boon by reaction between 9,10-phenanthrenequinone and 2-hydrazinopyridine in refluxing acetic acid.[7,8c] Neutralization produces a deep orange precipitate, which is recrystallized from acetic acid. Complexes **2**−**4** are readily prepared as microcrystalline precipitates by combination of a chloroform solution of **1** with a half-molar equivalents of $M(OAc)_2 \cdot H_2O$ in methanol. These precipitates feature nearly identical FTIR spectra, and the analytical data from combustion analysis also supports the purported 2:1 ligand-to-metal structural assignments. The molecular structures and packing of **2**−**4** are indicated in Figures 3−5, including a list of important bond distances and angles. All three complexes are pseudo-octahedral, featuring two coordinated tridentate PAPL anions binding through NNO donor sets. For complexes **2** and **4**, the coordinate bond distances to the central azo and terminal pyridine N atoms are longest and are approximately of the same length in each complex; the M−O bond is significantly shorter. Nickel complex **3** exhibits shorter coordinate bonds to the central and terminal N atoms and a slightly longer Ni−O bond, which is still shorter than the M−O bond distances observed for **2** and **4**. The N═N bond distances of the azo moiety range from 1.292 to 1.307 Å over all complexes, indicating significant double bond character.[5] Each of the C−O bonds is short over all three complexes; however, the distances are significantly longer than the C═O double bond distance (1.237(3) Å) reported in a related phenanthrol-based ligand.[19]

Electronic Properties. The electronic properties of compounds **1**−**4** in solution were investigated via a combination of UV−vis spectroscopy and cyclic voltammetry (CV) experiments. The room temperature electronic spectra of **1**−**4** are shown in Figure 6. Neutral and uncoordinated **1** exhibits a broad band in the visible region with a higher energy shoulder. These bands are assigned to two anticipated n−π* transitions of the azo substituent. Qualitatively speaking, the electronic spectra obtained from complexes **2**−**4** are similar to each other, featuring two longer wavelength visible bands accompanied by a higher energy shoulder. These bands are the result of ligand centered transitions (on the basis of TD-DFT calculation described in the next section), which are perturbed from **1** due to the presence of the metal cation. Complexes **3** and **4** feature very similar band shapes and intensities, while **2** exhibits weaker transitions, which were ascribed to weaker M−PAPL coordinate bonds in an earlier report; this is supported

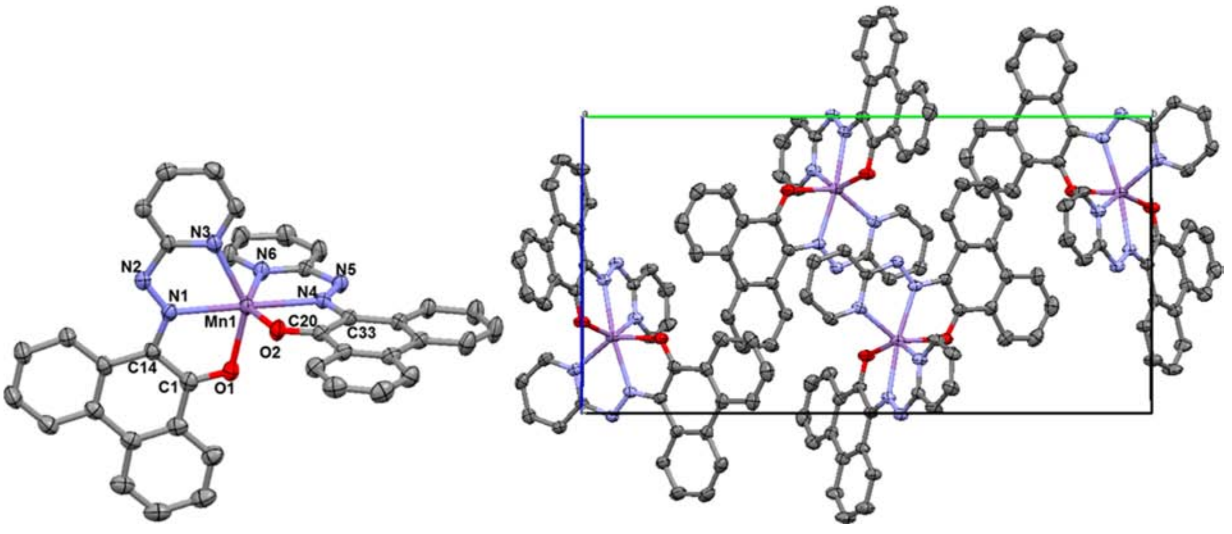

Figure 3. Left: Oak Ridge thermal ellipsoid plot (ORTEP) representation of the molecular structure of **2** with H atoms omitted. Thermal ellipsoids at 50% probability. Selected bond distances (Å) and angles (deg): Mn(1)−N(1), 2.2556(18); Mn(1)−N(3), 2.225(2); Mn(1)−N(6), 2.2231(19); Mn(1)−N(4), 2.2586(18); Mn(1)−O(1), 2.1391(17); Mn(1)−O(2), 2.1073(16); N(1)−N(2), 1.296(3); C(1)−O(1), 1.275(3); C(1)−C(14), 1.437(3); N(4)−N(5), 1.295(3); O(2)−C(20), 1.266(3); C(20)−C(33), 1.441(3) and N(4)−Mn(1)−N(1), 170.26(7); N(4)−Mn(1)−N(6), 69.93(7); N(1)−Mn(1)−N(6), 101.77(7); N(4)−Mn(1)−N(3), 114.38(7); N(1)−Mn(1)−N(3), 70.23(7); N(6)−Mn(1)−N(3), 93.03(7); N(4)−Mn(1)−O(2), 73.10(6); N(1)−Mn(1)−O(2), 115.53(6); N(6)−Mn(1)−O(2), 142.63(6); N(3)−Mn(1)−O(2), 97.21(7); N(4)−Mn(1)−O(1), 102.38(6); N(1)−Mn(1)−O(1), 72.66(6); N(6)−Mn(1)−O(1), 94.92(7); N(3)−Mn(1)−O(1), 142.89(6); O(2)−Mn(1)−O(1), 98.10(7). Right: Molecular packing of **2** viewed along the crystallographic a axis.

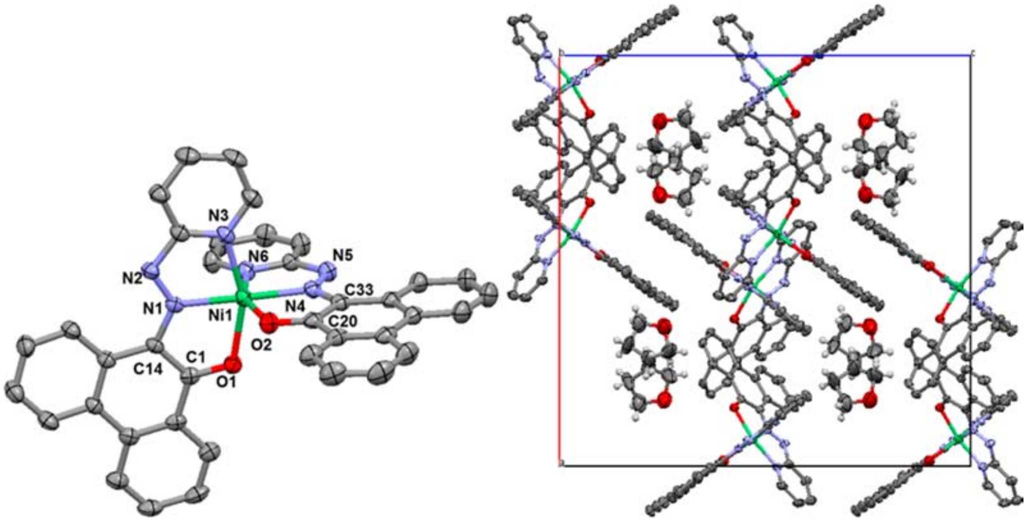

Figure 4. Left: ORTEP representation of the molecular structure of **3** with H atoms and single THF solvate molecule omitted. Thermal ellipsoids at 50% probability. Selected bond distances (Å) and angles (deg): Ni(1)−N(1), 2.007(3); Ni(1)−N(3), 2.056(3); Ni(1)−N(6), 2.051(3); Ni(1)−N(4), 2.007(3); Ni(1)−O(1), 2.067(2); Ni(1)−O(2), 2.062(2); N(1)−N(2), 1.298(4); C(1)−O(1), 1.276(4); C(1)−C(14), 1.430(5); N(4)−N(5), 1.307(4); O(2)−C(20), 1.265(4); C(20)−C(33), 1.430(5) and N(4)- Ni(1)−N(1), 178.65(11); N(4)−Ni(1)−N(6), 77.64(11); N(1)−Ni(1)−N(6), 101.40(11); N(4)−Ni(1)−N(3), 101.48(11); N(1)−Ni(1)−N(3), 77.59(11); N(6)−Ni(1)−N(3), 93.44(11); N(4)−Ni(1)−O(2), 79.11(10); N(1)−Ni(1)−O(2), 101.87(10); N(6)−Ni(1)−O(2), 156.70(10); N(3)−Ni(1)−O(2), 92.64(10); N(4)−Ni(1)−O(1), 101.93(10); N(1)−Ni(1)−O(1), 79.00(10); N(6)−Ni(1)−O(1), 91.52(10); N(3)−Ni(1)−O(1), 156.59(10); O(2)−Ni(1)−O(1), 91.77(9). Right: Molecular packing of **3** viewed along the crystallographic *b* axis (THF included).

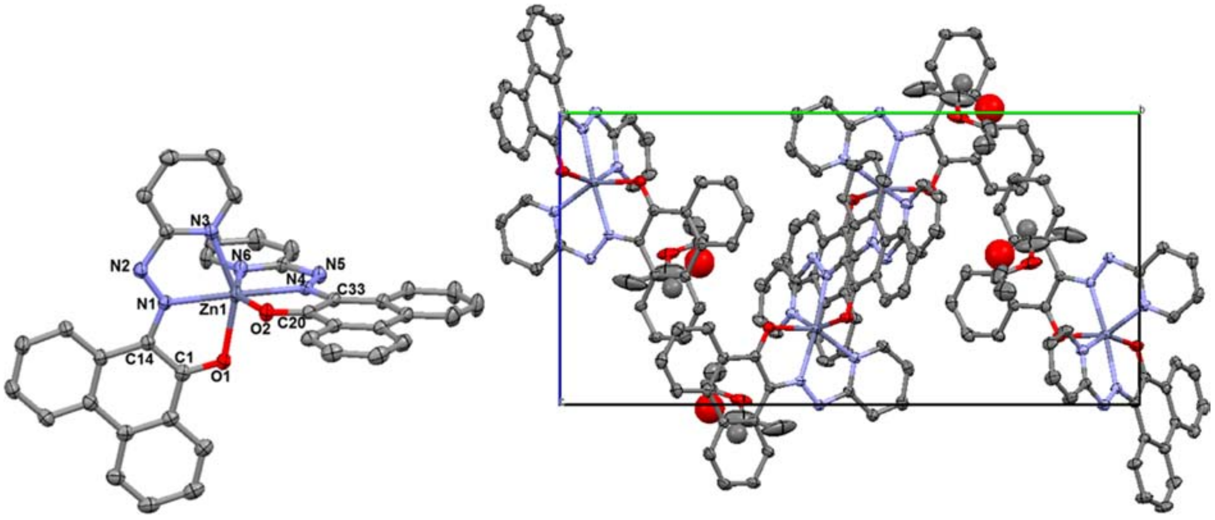

Figure 5. Left: ORTEP representation of the molecular structure of **4** with H atoms and diethyl ether molecule omitted. Thermal ellipsoids at 50% probability. Selected bond distances (Å) and angles (deg): Zn(1)−N(1), 2.1335(15); Zn(1)−N(3), 2.1365(17); Zn(1)−N(6), 2.1400(17); Zn(1)−N(4), 2.1405(15); Zn(1)−O(1), 2.1190(14); Zn(1)−O(2), 2.0881(14); N(1)−N(2), 1.292(2); C(1)−O(1), 1.272(2); C(1)−C(14), 1.435(3); N(4)−N(5), 1.302(2); O(2)−C(20), 1.260(2); C(20)−C(33), 1.448(3) and N(4)−Zn(1)−N(1), 174.04(6); N(4)−Zn(1)−N(6), 73.59(6); N(1)−Zn(1)−N(6), 101.60(6); N(4)−Zn(1)−N(3), 109.49(6); N(1)−Zn(1)−N(3), 73.98(6); N(6)−Zn(1)−N(3), 93.57(6); N(4)−Zn(1)−O(2), 76.41(5); N(1)−Zn(1)−O(2), 108.52(5); N(6)−Zn(1)−O(2), 149.86(6); N(3)−Zn(1)−O(2), 93.66(6); N(4)−Zn(1)−O(1), 100.98(6); N(1)−Zn(1)−O(1), 75.57(5); N(6)−Zn(1)−O(1), 93.96(6); N(3)−Zn(1)−O(1), 149.51(6); O(2)−Zn(1)−O(1), 94.48(6). Right: Molecular packing of **4** viewed along the crystallographic *a* axis (diethyl ether included).

by the X-ray structural data, which indicates very long Mn−PAPL coordinate bonds in **2**.

The electrochemical properties (Table 2) of compounds **2**−**4** were investigated by cyclic and square wave voltammetry, and the result for **2** is shown (Figure 7). The CV and SW data for **3** and **4** are provided in the Supporting Information (Figures S1−S4). For **2**−**4**, all of the electrochemical data is suggestive of two closely spaced cathodic processes of varying degrees of reversibility and two irreversible anodic processes (three for **2**). The first two cathodic processes can be assigned to two ligand-centered (azo) reductions to produce two coordinated dianion radical species followed by a subsequent irreversible two-electron (based on current) reduction, likely resulting in N−N bond cleavage and decomposition. The first anodic process is assigned to a ligand centered oxidation (oxidation of the phenoxide O to phenoxyl radical), and the higher potential irreversible wave is subsequent oxidation to quinone. For **2**, the first anodic process (+0.7 V) is attributed to oxidation of Mn^{2+}.

The solid-state temperature dependent magnetic properties of neutral complex **3** were investigated using SQUID

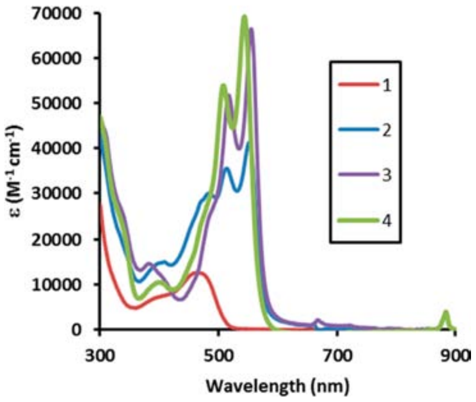

Figure 6. Room temperature UV−vis spectra of **1**−**4** in CH_2Cl_2.

Table 2. Selected Electrochemical Data^{a}

complex	$E'_{1/2}{}^{b}$ (V) or $E_{pa}/E_{pc}{}^{c}$
2	$+0.7^{qr}$, $+1.2^{irr}$, $+1.6^{irr}$, −0.9, −1.2, -1.6^{irr}
3	$+1.0^{irr}$, $+1.3^{irr}$, −1.0, −1.3, -1.9^{irr}
4	$+1.0^{irr}$, $+1.2^{irr}$, -1.0^{qr}, -1.3^{qr}, -1.8^{irr}

^{a}All experiments were performed in CH_3CN, containing 0.1 M $^{n}Bu_4NPF_6$ supporting electrolyte, and all potentials are quoted versus Ag/AgCl reference. $^{b}E'_{1/2} = (E_{pa} + E_{pc})/2$. $^{c}E_{pa}/E_{pc}$ are reported for irreversible (irr) or quasireversible (qr) processes.

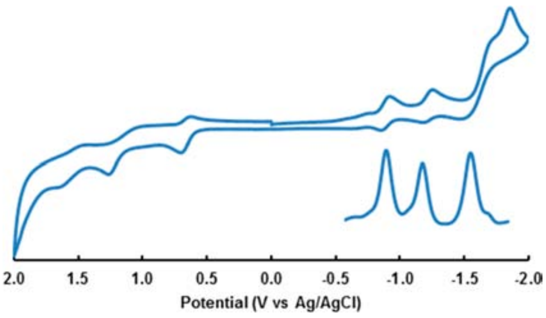

Figure 7. Cyclic voltammogram of a 10^{-3} M solution **2** in CH_3CN containing approximately 0.1 M Bu_4NPF_6 with a scan rate of 100 mV/s. Inset, cathodic square wave voltammogram of **2**.

Table 3. Selected Calculated Metrical Parameters for 3 (Observed Value, Averaged in Some Instances)

bond	Å	angle	deg
Ni—O	2.085 (2.065)	O—Ni—N_{py}	92.35 (92.08)
Ni—N_{azo}	2.052 (2.007)	O—Ni—N_{py}	154.83 (156.65)
Ni—N_{py}	2.112 (2.054)	O—Ni—N_{azo}	78.11 (79.06)
N=N	1.295 (1.302)	O—Ni—N_{azo}	100.89 (101.9)
C—O	1.259 (1.270)	O—Ni—O	91.68 (91.77)
		N_{py}—Ni—N_{azo}	76.73 (77.62)
		N_{azo}—Ni—N_{azo}	178.59 (178.65)
		N_{py}—Ni—N_{py}	94.48 (93.44)

magnetometry, and the data is available in the Supporting Information as a plot of $\chi_m T$ versus temperature (Supporting Information Figure S5). These data can be described by typical "spin-only" behavior ($S = 1$, $\chi_m T = 1.08$ cm^3 mol^{-1} K), with minor deviations due to zero-field splitting and/or very weak antiferromagnetic intermolecular magnetic exchange interactions, which are observed only at very low temperatures (<10 K). The room temperature magnetic moment of complex **2** is 5.92 μ_B, and the variable temperature magnetic properties of this complex were not studied since spin-only behavior, as observed for **3**, is anticipated. Zinc complex **4** is diamagnetic at room temperature, as expected.

Spectroelectrochemistry. Spectroelectrochemical experiments were performed on complexes **2** and **3** (the quasireversibility of the cathodic waves in **4** indicated a nonviable reduction) in acetonitrile solvent, and the results are displayed in Figure 8. For complexes **2** and **3**, potentials of −1.0, −1.2, and −1.5 V were applied, corresponding to the ligand-centered reductions identified by cyclic voltammetry. At a potential of −1.0 V for **2**, changes to the visible spectra with time indicated decomposition with the limiting spectrum very closely resembling that of the uncoordinated ligand **1**. When the potential was lowered to −1.2 V for complex **2**, a very rapid decrease in absorbance at 548 and 513 nm was noted, with concomitant growth of new bands at 603, 484, and 328 nm (Figure 8). Given the decomposition noted at −1.0 V, we suspect that the changes in the visible spectrum observed at −1.2 V are also the result of complex decomposition, and we speculate that the spectral features may result from reduction of the decomplexed PAPL ligand. No significant changes to the visible spectrum of **3** were indicated at potentials of −1.0 or −1.2 V. At a potential of −1.5 V, absorption intensity at 549,

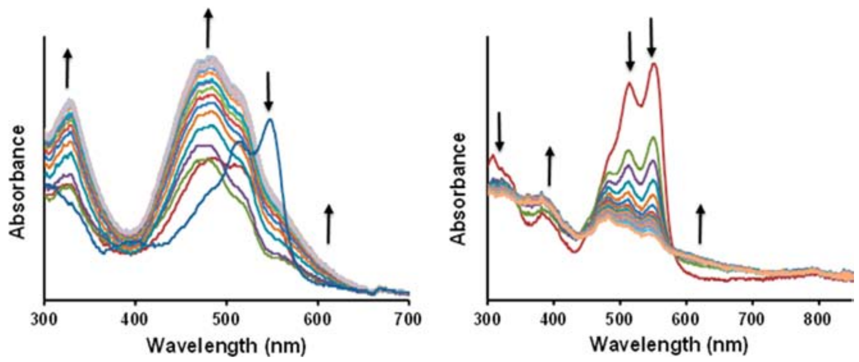

Figure 8. Spectroelectrochemical data for **2** (left, at a potential of +1.2 V) and **3** (right, at a potential of +1.5 V) in CH_3CN.

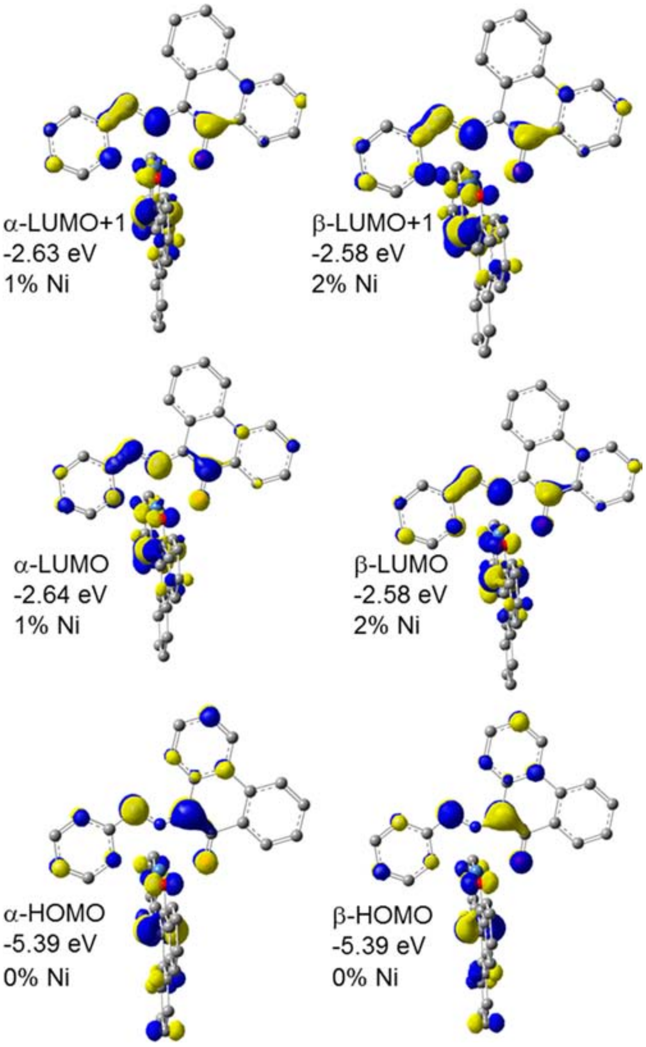

Figure 9. *α*- and *β*-HOMO, LUMO, and LUMO + 1 with relative energies and percent Ni composition calculated at the B3LYP/TZVP level of theory for **3**.

Table 4. TD-DFT Calculated Spectral Data for 3

transition number	nm	*ϕ*	assignment
8	549.5	0.0009	*α*-HOMO → *α*-LUMO (50%)
			α-HOMO − 1 → *α*-LUMO + 1 (50)
9	549.4	0.0008	*α*-HOMO → *α*-LUMO + 1 (52)
			α-HOMO − 1 → *α*-LUMO (48)
10	543.1	0.0002	*β*-HOMO → *β*-LUMO (50)
			β-HOMO − 1 → *β*-LUMO + 1 (50)
11	542.8	0.0002	*β*-HOMO → *β*-LUMO + 1 (50)
			β-HOMO − 1 → *β*-LUMO (50)
12	495.3	0.0160	*β*-HOMO − 6 → *β*-LUMO + 6 (38)
			β-HOMO − 5 → *β*-LUMO + 7 (24)
13	495.2	0.0272	*β*-HOMO − 5 → *β*-LUMO + 6 (34)
			β-HOMO − 6 → *β*-LUMO + 7 (28)
14	478.7	0.1401	*β*-HOMO − 12 → *β*-LUMO + 7 (20)
15	476.7	0.4196	*α*-HOMO − 1 → *α*-LUMO (27)
			β-HOMO − 1 → *β*-LUMO (26)
			β-HOMO → *β*-LUMO + 1 (23)
			α-HOMO → *α*-LUMO + 1 (20)
16	473.4	0.2173	*β*-HOMO − 1 → *β*-LUMO + 1 (18)
			α-HOMO − 1 → *α*-LUMO + 1 (18)
			β-HOMO − 12 → *β*-LUMO + 7 (16)
			β-HOMO → *β*-LUMO (12)
			α-HOMO → *α*-LUMO (12)
19	426.1	0.0205	*α*-HOMO − 5 → *α*-LUMO (83)
20	425.6	0.0190	*α*-HOMO − 5 → *α*-LUMO + 1 (85)
23	400.7	0.1540	*α*-HOMO − 4 → *α*-LUMO (26)
			α-HOMO − 3 → *α*-LUMO + 1 (25)
			β-HOMO − 3 → *β*-LUMO (25)
			β-HOMO − 2 → *β*-LUMO + 1 (24)
24	400.2	0.0412	*α*-HOMO − 3 → *α*-LUMO (26)
			α-HOMO − 4 → *α*-LUMO + 1 (25)
			β-HOMO − 2 → *β*-LUMO (25)
			β-HOMO − 3 → *β*-LUMO + 1 (24)

512, and 319 nm decreased for complex **3**, with new absorptions observed at 618, 480, and 378 nm. Given that the low energy absorptions (>500 nm) for **3** involve ligand-centered molecular orbitals featuring significant azo character, it is reasonable that the absorption intensity of these bands should decrease upon reduction, which would result in a loss of azo character. While the reduced spectra of **2** and **3** do share some similarities (new absorptions at approximately 480 and 600 nm), the decrease in absorbance with time occurs much more slowly in **3** than in **2**, and the new absorption bands in **3** are much weaker in intensity than the bands that appeared in **2**. Also, when we cease applying the −1.5 V potential to the solution of complex **3**, we slowly regenerate the visible spectrum of neutral **3**, indicating that the complex is not undergoing the same decomposition pathway that we observed with **2**. It appears that by applying a potential of −1.5 V we can reversibly generate a solution of the doubly reduced complex $\mathbf{3}^{2-}$. We could find two examples of cathodic spectroelec-

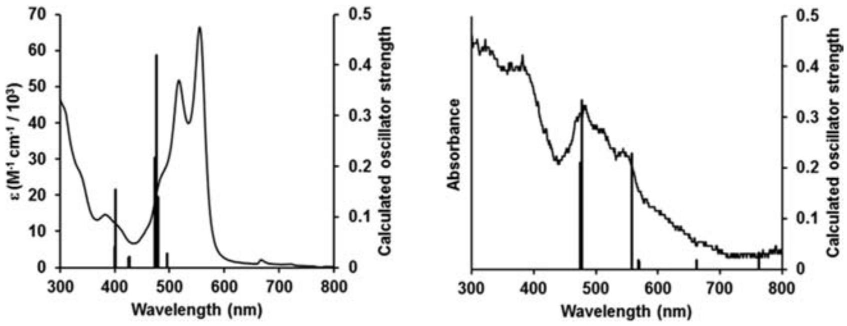

Figure 10. Experimental (curve) and calculated (bars) electronic spectra of **3** (left) and spectroelectrochemically generated $\mathbf{3}^{2-}$ (S = 2, right) calculated at the B3LYP/TZVP level of theory (TD-DFT).

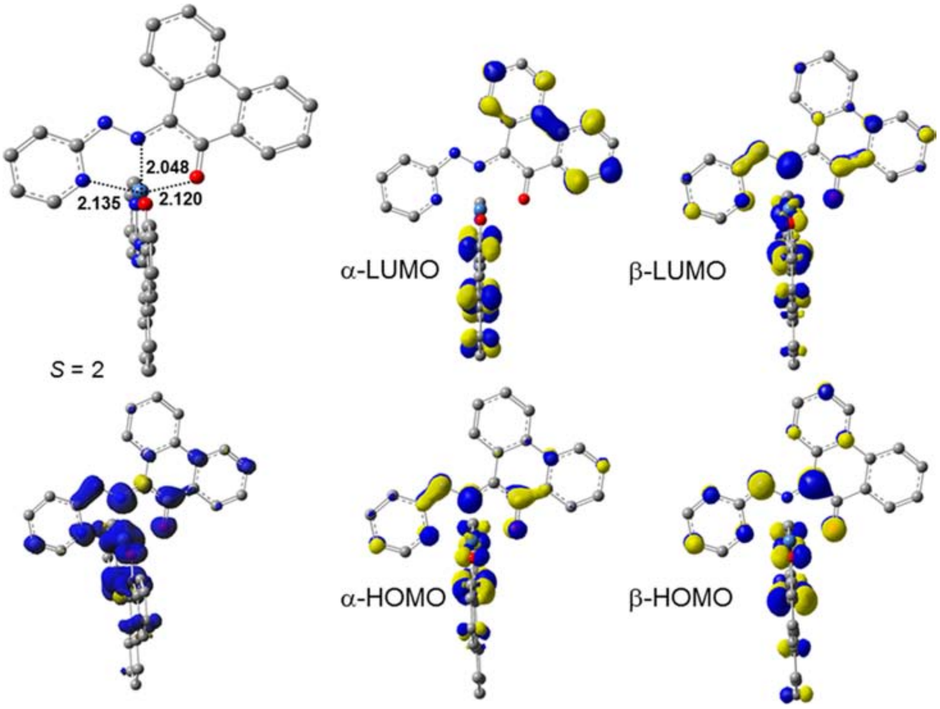

Figure 11. (Left) Optimized geometry (top) and spin density distribution (bottom). (Right) Frontier molecular orbitals for 3^{2-} in the $S = 2$ state calculated at the B3LYP/TZVP level of theory.

Table 5. TD-DFT Calculated Spectral Data for 3^{2-}

transition number	nm	ϕ	assignment
4	762.8	0.0284	α-HOMO → α-LUMO + 2 (64%) α-HOMO − 1 → α-LUMO + 3 (36)
5	762.6	0.0330	α-HOMO − 1→ α-LUMO + 2 (60) α-HOMO → α-LUMO + 3 (40)
11	662.5	0.0177	α-HOMO − 1 → α-LUMO + 5 (52) α-HOMO → α-LUMO + 4 (48)
14	569.2	0.0153	α-HOMO − 1 → α-LUMO + 4 (52) α-HOMO → α-LUMO + 5 (48)
15	568.8	0.0179	α-HOMO − 1 → α-LUMO + 5 (52) α-HOMO → α-LUMO + 4 (48)
16	557.3	0.2275	β-HOMO − 1 → β-LUMO (45) β-HOMO → β-LUMO + 1 (45)
17	557.2	0.1907	β-HOMO → β-LUMO (52) β-HOMO − 1 → β-LUMO + 1 (35)
22	477.4	0.3333	α-HOMO − 1 → α-LUMO + 6 (51) α-HOMO → α-LUMO + 7 (49)
23	474.7	0.2107	α-HOMO → α-LUMO + 6 (55) α-HOMO − 1 → α-LUMO + 7 (45)

trochemistry on homoleptic first row transition metal complexes (Mn^{2+} or Fe^{3+}) containing other 2-(arylazo)pyridine ligands (Figure 1 right, R = H, CH_3), and by in large the results are in line with the data we have observed with complex **3**.[6]

DFT/TD-DFT Calculations. DFT calculations were used to probe the electronic structure of the $Ni(PAPL)_2$ complex as well as the hypothetical doubly reduced $[Ni(PAPL)_2]^{2-}$ complexes in both the $S = 0$ or 2 states, which correspond to nickel–ligand magnetic coupling that is anti- or ferromagnetic in nature, respectively. The structure of neutral complex **3** was first optimized (B3LYP/TZVP), and the gross structural features, including coordinate bond distances and angles, compare fairly well with the experimental X-ray data (Table 3). Coordinate bond lengths are calculated to be longest between Ni and the terminal pyridine ring nitrogen atom, which is at odds somewhat with the X-ray data, which indicated longest Ni–O coordinate bonds. However, the calculated N═N and C—O bond distances also agree well with the experimentally observed data. The calculated α- and β-LUMO (and α- or β-LUMO + 1) for complex **3** are shown in Figure 8 and are delocalized molecular orbitals with significant coefficients on the azo groups of the PAPL ligands, as anticipated, and very little nickel participation is evident. This LUMO structure supports the aforementioned electrochemical assignments that suggested the first two cathodic waves result from reduction of the ligand to produce coordinated radical dianions. The calculated α- and β-HOMOs (Figure 9) are also delocalized over the ligand with no contribution from nickel ion. The electronic absorption spectra of **3** was calculated using TD-DFT at the same level as theory (Figure 10, left). Intense transitions are calculated for the visible region of the spectrum for **3**, which qualitatively agrees with the experimentally observed data; however, the calculated transition energies are quite different from the observed values. Calculated lower-energy transitions (549 and 543 nm; see Table 4 for selected TDDFT data) involve ligand centered frontier molecular orbitals (α- or β- HOMO or HOMO − 1), and can be classified as intraligand charge transfer bands (ILCT). Data for all the calculated transitions can be found in the Supporting Information (Table S1).

We also optimized the geometries of the hypothetical doubly reduced complex 3^{2-} in the two possible spin states, $S = 0$ or 2, corresponding to anti- or ferromagnetic metal–ligand magnetic coupling, respectively (Figure 11). In the $S = 0$ state, nickel ($S = 1$) is antiferromagnetically coupled to two ligand radical dianions ($2 \times S = {}^{1}/_{2}$); in the $S = 2$ state, nickel is ferromagnetically coupled to two ligand radical dianions. DFT calculations of the electronic states with anti- or ferromagnetic metal−ligand magnetic coupling at their respective optimized geometries indicate that the $S = 2$ state is the lowest-energy state and the $S = 0$ state is 909 cm^{-1} above the ground state. These calculated data suggest strong ferromagnetic magnetic exchange coupling in the doubly reduced state. The lower energy of the $S = 2$ state is likely the result of the planar PAPL chelate, which results in an orthogonal magnetic orbital arrangement between the σ-type magnetic orbitals of nickel (d_{z^2} and $d_{x^2-y^2}$) and the π-type nature of the reduced PAPL ligand. The visible spectrum of $\mathbf{3}^{2-}$ in the $S = 2$ state was calculated, and these data compare well with the data from the spectroelectrochemically generated $\mathbf{3}^{2-}$. Lower energy transitions are calculated at 763, 662, and 569 nm which all originate from the ligand-centered α-HOMO or α-HOMO − 1 (Table 5 and Supporting Information Table S2). Intense transitions are calculated at 557, 477, and 474 cm^{-1}, which agree well with the experimental data. These transitions all originate from the α- or β-HOMO or HOMO − 1.

■ CONCLUSIONS

We have initiated a study of the structural and electronic properties of complexes containing the redox active ligand 1-(2-pyridylazo)-2-phenanthrol (PAPL). Complexes are reversibly reduced at negative potentials and feature intense ligand centered visible absorption bands. Spectroelectrochemical measurements suggest decomposition for complex **2**; however, measurements on complex **3** in concert with TD-DFT calculations on the purported doubly reduced complex suggest formation of a nickel-radical complex. While this complex is not yet isolable in our hands, DFT calculations do indicate a well isolated high spin ground state for this material. We are currently exploring polytopic derivatives of the PAPL framework featuring reduced reduction potentials, and will report on transition metal or lanthanide complexes containing these ligands in due course.

■ ASSOCIATED CONTENT

Ⓢ Supporting Information

Crystallographic data files (CIF format), electrochemical data for **3** and **4**, magnetic data for **3**, and calculated visible spectral details for **3** and $\mathbf{3}^{2-}$. This material is available free of charge via the Internet at http://pubs.acs.org.

■ AUTHOR INFORMATION

Corresponding Author

*E-mail: lemairem@brandonu.ca.

Notes

The authors declare no competing financial interest.

■ ACKNOWLEDGMENTS

We thank the Natural Sciences and Engineering Research Council of Canada, the Canada Foundation for Innovation, and the Canada Research Chairs program for support. Dr. Paul A. Dube (Brockhouse Institute for Materials Research, McMaster University) is acknowledged for running the variable temperature magnetic susceptibility measurement.

■ REFERENCES

(1) (a) Luca, O. R.; Crabtree, R. H. *Chem. Soc. Rev.* **2013**, *42*, 1440. (b) Praneeth, V. K. K.; Ringenberg, M. R.; Ward, T. R. *Angew. Chem., Int. Ed.* **2012**, *51*, 10228−10234. (c) Zhu, D.; Thapa, I.; Korobkov, I.; Gambarotta, S.; Budzelaar, P. H. M. *Inorg. Chem.* **2012**, *50*, 9879−9887.

(2) Kaim, W.; Schwederski, B. *Coord. Chem. Rev.* **2012**, *254*, 1580−1588.

(3) (a) Paul, N. D.; Rana, U.; Goswami, S.; Mondal, T. K.; Goswami, S. *J. Am. Chem. Soc.* **2012**, *134*, 6520−6523. (b) Joy, S.; Pal, P.; Mondal, T. K.; Talapatra, G. B.; Goswami, S. *Chem.—Eur. J.* **2012**, *18*, 1761−1771.

(4) (a) Paul, N. D.; Samanta, S.; Mondal, T. K.; Goswami, S. *Inorg. Chem.* **2011**, *50*, 7886−7893. (b) Joy, S.; Kramer, T.; Paul, N. D.; Banerjee, P.; McGrady, J. E.; Goswami, S. *Inorg. Chem.* **2011**, *50*, 9993−10004. (c) Sanyal, A.; Chatterjee, S.; Castineiras, A.; Sarkar, B.; Singh, P.; Fiedler, J.; Záliš, S.; Kaim, W.; Goswami, S. *Inorg. Chem.* **2007**, *46*, 8584−8593.

(5) Samanta, S.; Ghosh, P.; Goswami, S. *Dalton Trans.* **2012**, *41*, 2213−2226.

(6) (a) Saha, A.; Majumdar, P.; Peng, S.-M.; Goswami, S. *Eur. J. Inorg. Chem.* **2000**, 2631−2639. (b) Saha, A.; Majumdar, P.; Goswami, S. *J. Chem. Soc., Dalton Trans.* **2000**, 1703−1708.

(7) Chiswell, B.; Lions, F.; Tomlinson, M. L. *Inorg. Chem.* **1964**, *3*, 492−499.

(8) (a) Bhoon, Y. K.; Pandeya, K. B.; Singh, R. P. *Indian J. Chem.* **1975**, *13*, 84−85. (b) Pandeya, K. B.; Singh, R. P.; Bhoon, Y. K. *Indian J. Chem.* **1976**, *14A*, 681−682. (c) Pandeya, K. B.; Singh, R. P.; Bhoon, Y. K. *J. Coord. Chem.* **1976**, *6*, 71−74. (d) Bhoon, Y. K.; Pandeya, K. B.; Singh, R. P. *Bull. Soc. Chim. Fr.* **1979**, 104−107. (e) Bhoon, Y. K.; Singh, R. P.; Gregson, A. K. *J. Coord. Chem.* **1979**, *9*, 251−253. (f) Pandeya, K. B.; Singh, R. P.; Sawhney, G. L.; Baijal, J. S. *Solid State Commun.* **1979**, *32*, 823−825. (g) Mochizuki, K.; Fujimoto, M. *Chem. Lett.* **1980**, 1541−1544. (h) Mochizuki, K.; Fujimoto, M. *Bull. Chem. Soc. Jpn.* **1985**, *58*, 1520−1523.

(9) (a) Mukhopadhyay, S.; Ray, D. *J. Chem. Soc., Dalton Trans.* **1995**, 265−268. (b) Mondal, P.; Hens, A.; Basak, S.; Rajak, K. K. *Dalton Trans.* **2013**, *42*, 1536−1549.

(10) Frisch, M. J.; Trucks, G. W.; Schlegel, H. B.; Scuseria, G. E.; Robb, M. A.; Cheeseman, J. R.; Scalmani, G.; Barone, V.; Mennucci, B.; Petersson, G. A.; Nakatsuji, H.; Caricato, M.; Li, X.; Hratchian, H. P.; Izmaylov, A. F.; Bloino, J.; Zheng, G.; Sonnenberg, J. L.; Hada, M.; Ehara, M.; Toyota, K.; Fukuda, R.; Hasegawa, J.; Ishida, M.; Nakajima, T.; Honda, Y.; Kitao, O.; Nakai, H.; Vreven, T.; Montgomery, J. A., Jr.; Peralta, J. E.; Ogliaro, F.; Bearpark, M.; Heyd, J. J.; Brothers, E.; Kudin, K. N.; Staroverov, V. N.; Kobayashi, R.; Normand, J.; Raghavachari, K.; Rendell, A.; Burant, J. C.; Iyengar, S. S.; Tomasi, J.; Cossi, M.; Rega, N.; Millam, J. M.; Klene, M.; Knox, J. E.; Cross, J. B.; Bakken, V.; Adamo, C.; Jaramillo, J.; Gomperts, R.; Stratmann, R. E.; Yazyev, O.; Austin, A. J.; Cammi, R.; Pomelli, C.; Ochterski, J. W.; Martin, R. L.; Morokuma, K.; Zakrzewski, V. G.; Voth, G. A.; Salvador, P.; Dannenberg, J. J.; Dapprich, S.; Daniels, A. D.; Farkas, Ö.; Foresman, J. B.; Ortiz, J. V.; Cioslowski, J.; Fox, D. J. *Gaussian 09, Revision A.02*; Gaussian, Inc.: Wallingford, CT, 2009.

(11) Becke, A. D. *J. Chem. Phys.* **1993**, *98*, 5648−5652.

(12) Lee, C.; Yang, W.; Parr, R. G. *Phys. Rev.* **1988**, *B37*, 785−789.

(13) Schafer, A.; Huber, C.; Ahlrichs, R. *J. Chem. Phys.* **1994**, *100*, 5829−5835.

(14) Reed, A. E.; Curtiss, L. A.; Weinhold, F. *Chem. Rev.* **1988**, *88*, 899−926.

(15) Mayer, I. *Int. J. Quantum Chem.* **1986**, *29*, 73−84.

(16) Gorelsky, S. I.; Basumallick, L.; Vura-Weis, J.; Sarangi, R.; Hedman, B.; Hodgson, K. O.; Fujisawa, K.; Solomon, E. I. *Inorg. Chem.* **2005**, *44*, 4947−4960.

(17) Gorelsky, S. I. *AOMix Version 6.6*; University of Ottawa: Ottawa, Canada, 2012.

(18) Gorelsky, S. I.; Lever, A. B. P. *J. Organomet. Chem.* **2001**, *635*, 187−196.

(19) Davydov, V. V.; Sokol, V. I.; Polyanskaya, N. A.; Linko, R. V.; Ryabov, M. A.; Sergienko, V. S. *Crystallogr. Rep.* **2012**, *57*, 227−234.